

Linear dichroism transition and polarization-sensitive photodetector of quasi-one-dimensional palladium bromide

Wan-Li Zhu(朱万里), Wei-Li Zhen(甄伟立), Rui Niu(牛瑞), Ke-Ke Jiao(焦珂珂), Zhi-Lai Yue(岳智来), Hui-Jie Hu(胡慧杰), Fei Xue(薛飞), and Chang-Jin Zhang(张昌锦)

Citation: Chin. Phys. B, 2024, 33 (**6**): 068101. DOI: 10.1088/1674-1056/ad36ba
Journal homepage: http://cpb.iphy.ac.cn; http://iopscience.iop.org/cpb

What follows is a list of articles you may be interested in

Experimental investigation of omnidirectional multiphysics bilayer invisibility cloak with anisotropic geometry

Huolei Feng(丰火雷), Xingwei Zhang(张兴伟), Limin Zhou(周利敏), Yuekai Zhang(张悦凯), and Yushan Ni(倪玉山)
Chin. Phys. B, 2024, 33 (**3**): 038102. DOI: 10.1088/1674-1056/acf490

Effect of interface anisotropy on tilted growth of eutectics: A phase field study

Mei-Rong Jiang(姜美荣), Jun-Jie Li(李俊杰), Zhi-Jun Wang(王志军), and Jin-Cheng Wang(王锦程)
Chin. Phys. B, 2022, 31 (**10**): 108101. DOI: 10.1088/1674-1056/ac76af

Numerical simulation on dendritic growth of Al-Cu alloy under convection based on the cellular automaton lattice Boltzmann method

Kang-Wei Wang(王康伟), Meng-Wu Wu(吴孟武), Bing-Hui Tian(田冰辉), and Shou-Mei Xiong(熊守美)
Chin. Phys. B, 2022, 31 (**9**): 098105. DOI: 10.1088/1674-1056/ac7211

Numerical study of growth competition between twin grains during directional solidification by using multi-phase field method

Chang-Sheng Zhu(朱昶胜), Ting Wang(汪婷), Li Feng(冯力), Peng Lei(雷鹏), and Fang-Lan Ma(马芳兰)
Chin. Phys. B, 2022, 31 (**2**): 028102. DOI: 10.1088/1674-1056/ac0eed

Electronic, optical property and carrier mobility of graphene, black phosphorus, and molybdenum disulfide based on the first principles

Congcong Wang(王聪聪), Xuesheng Liu(刘学胜), Zhiyong Wang(王智勇), Ming Zhao(赵明), Huan He(何欢), Jiyue Zou(邹吉跃)
Chin. Phys. B, 2018, 27 (**11**): 118106. DOI: 10.1088/1674-1056/27/11/118106

Linear dichroism transition and polarization-sensitive photodetector of quasi-one-dimensional palladium bromide

Wan-Li Zhu(朱万里)[1,2], Wei-Li Zhen(甄伟立)[1,†], Rui Niu(牛瑞)[1], Ke-Ke Jiao(焦珂珂)[1], Zhi-Lai Yue(岳智来)[1], Hui-Jie Hu(胡慧杰)[1], Fei Xue(薛飞)[3], and Chang-Jin Zhang(张昌锦)[1,4,‡]

[1] *Anhui Key Laboratory of Low-energy Quantum Materials and Devices, High Magnetic Field Laboratory, HFIPS, Chinese Academy of Sciences, Hefei* 230031, *China*

[2] *Science Island Branch, Graduate School of University of Science and Technology of China, Hefei* 230026, *China*

[3] *School of Physics, Hefei University of Technology, Hefei* 230601, *China*

[4] *Collaborative Innovation Center of Advanced Microstructures, Nanjing University, Nanjing* 210093, *China*

(Received 18 December 2023; revised manuscript received 28 February 2024; accepted manuscript online 22 March 2024)

Perpendicular optical reversal of the linear dichroism transition has promising applications in polarization-sensitive optoelectronic devices. We perform a systematical study on the in-plane optical anisotropy of quasi-one-dimensional $PdBr_2$ by using combined measurements of the angle-resolved polarized Raman spectroscopy (ARPRS) and anisotropic optical absorption spectrum. The analyses of ARPRS data validate the anisotropic Raman properties of the $PdBr_2$ flake. And anisotropic optical absorption spectrum of $PdBr_2$ nanoflake demonstrates distinct optical linear dichroism reversal. Photodetector constructed by $PdBr_2$ nanowire exhibits high responsivity of 747 $A{\cdot}W^{-1}$ and specific detectivity of 5.8×10^{12} Jones. And the photodetector demonstrates prominent polarization-sensitive photoresponsivity under 405-nm light irradiation with large photocurrent anisotropy ratio of 1.56, which is superior to those of most of previously reported quasi-one-dimensional counterparts. Our study offers fundamental insights into the strong optical anisotropy exhibited by $PdBr_2$, establishing it as a promising candidate for miniaturization and integration trends of polarization-related applications.

Keywords: linear dichroism reversal, polarization sensitivity, anisotropy, polarized photodetector

PACS: 81.05.Hd, 81.07.Gf, 85.30.De, 85.60.Gz **DOI:** 10.1088/1674-1056/ad36ba

1. Introduction

Optical information detection has always been a primary way for humans to perceive the external world.[1] Light is an electromagnetic wave that consists of key elements information like intensity, wavelength, phase, and polarization.[2] Polarized light detection technology plays an important role in the fields of optical fiber communication, environmental monitoring, and remote imaging.[3–5] In contrast to traditional photodetectors, polarized photodetectors show the ability to extract light polarization to provide more and clearer information about the imaged objects (*e.g.*, surface roughness, geometry or orientation).[6–8] The development of polarization-sensitive devices is of crucial importance for meeting with the requirements of miniaturization, compactness, and high integration.[9,10]

The versatility and engineerability of low-dimensional materials enable them to play superior roles in development of polarization-sensitive devices.[4,11–13] For instance, by combining different types of low-dimensional materials, the spectral response range of opto-devices can be significantly broadened.[14–18] And low-dimensional materials can affect their physical properties through surface defect states or local fields,[19–21] which provide opportunities to optimize polarized light detectors. Nanowire-based polarized photodetectors have gained significant recognition for their compact device size, exceptional conversion efficiency, adjustable light absorption coefficient, and wide spectral range.[22–29] This is particularly important in the context of industrial market demand for device integration and miniaturization. Searching for new polarization-sensitive low-dimensional materials has long been a research frontier.

Low-dimensional transition metal halides (TMHs) have received much attention due to their diverse optoelectronic properties,[30,31] topological magneton and electromagnetic properties,[32–34] and broad applications in spintronics.[35,36] Palladium bromide ($PdBr_2$), a recently reported TMH with quasi-one-dimensional structure, has become the center of research due to its ultrahigh current carrying capacity,[37] bipolar magnetic semiconducting properties,[38] and ultrasensitive photoresponse for photodetectors and field-effect transistors.[39] Here, we present experiments systematically revealing in-plane optical anisotropy of $PdBr_2$, including the angle resolved polarized Raman spectroscopy (ARPRS), and

†Corresponding author. E-mail: wlzhen@mail.ustc.edu.cn
‡Corresponding author. E-mail: zhangcj@hmfl.ac.cn

© 2024 Chinese Physical Society and IOP Publishing Ltd

anisotropic optical absorption spectrum. The ARPRS data validate the anisotropic phonon vibration properties and the crystal structure orientation of the $PdBr_2$ flake. And the angle-resolved absorption spectrum of the $PdBr_2$ nanoflake reveals the in-plane anisotropic optical properties. A peculiar occurrence of polarization reversal is detected at 397 nm, exhibiting perpendicular optical linear dichroism (LD) reversal. High-performance polarization photodetector constructed by $PdBr_2$ nanowire has been achieved, which exhibits responsivity of 747 $A{\cdot}W^{-1}$, specific detectivity of 5.8×10^{12} Jones and strong polarization-sensitive photoresponsivity (photocurrent anisotropic ratio of 1.56) under the 405-nm light irradiation, respectively. Our study offers essential insights into the optical anisotropy exhibited by $PdBr_2$. The remarkable anisotropic characteristics and semiconductor nature make $PdBr_2$ a captivating contender for applications involving polarization imaging, which facilitates the exploration of downsizing trends in polarization-resolved detectors and expands the potential applications of quasi-one-dimensional materials towards the advancement of optoelectronic devices with low-dimensional polarization sensitivity in the future.

2. Experiment

Needle-like single crystals of $PdBr_2$ were synthesized through the physical vapor transport (PVT) method. An evacuated quartz tube was utilized to contain 200 mg of $PdBr_2$ powder (with purity of 99.99%, purchased from Alfa Aesar) under vacuum condition ($< 10^{-4}$ Torr, 1 Torr = 1.33322×10^2 Pa). The tube was positioned within a horizontal double-zone tube furnace, with the source and growth zones being heated to 973 K and 673 K, respectively. The tube was kept at these temperatures for 7 days and then cooled down naturally.

A Rigaku-TTR3 x-ray diffractometer with Cu $K\alpha$ radiation was used for single crystal x-ray diffraction measurements. The angle-resolved polarized Raman spectroscopy measurements were conducted using a Horiba Jobin Yvon confocal Raman spectrometer (LabRam800HR). The polarized absorption spectra of the nanoflake sample was collected using a micro-zone absorption spectrometer (MStarter ABS, Metatest Co. Ltd.). The two-terminal devices were fabricated by transferring the $PdBr_2$ channel material to the pre-prepared electrodes using polydimethylsiloxane (PDMS) as the carrier. Figure S1 shows the optical microscope image of the mechanically exfoliated $PdBr_2$ nanoflakes and nanowires on a PDMS substrate. The ease of stripping $PdBr_2$ into nanowires could be due to its quasi-one-dimensional chain structure. The electrical and optoelectronic measurements were carried out using a home-made multi measurement system equipped with a Keithley 2636B source meter and a four-probe station. The 405-nm polarized laser was obtained through a Glan Taylor prism and a half wave plate. The power of the incident laser was calibrated by a power meter (PM100D, Thorlabs), and the laser spot diameter of 5 mm was sufficient to uniformly cover the entire device channel area.

3. Results and discussion

Figure 1(a) displays the schematic structure of $PdBr_2$ with different view directions. $PdBr_2$ belongs to the monoclinic crystal structure with the space group $P2_1/c$ (No. 14, $a = 6.59$ Å, $b = 3.96$ Å, $c = 25.22$ Å, and α, $\gamma = 90°$, $\beta = 92.6°$). In this structure, weak van der Waals interactions bundle together one-dimensional (1D) chains that solely possess covalent bonds along chain direction. Single crystal x-ray diffraction patterns of the obtained grown samples showed sharp diffraction peaks (Fig. 1(b)) that matched well with the standard PDF card (PDF#76-1621) of $PdBr_2$ crystal, indicating the high crystallinity. The length of the obtained $PdBr_2$ single crystals could be longer than 1 cm, as shown in the inset of Fig. 1(b). To comprehensively investigate the electronic properties of monoclinic $PdBr_2$, we calculated the band structure of bulk $PdBr_2$. The results are shown in Fig. 1(c). First-principles calculations are executed using the density functional theory (DFT) framework, employing projector augmented wave (PAW) potentials as implemented in the Vienna *ab initio* simulation package (VASP). For the structural relaxation part of the DFT calculations, we utilize the generalized gradient approximation (GGA) as formulated by Perdew, Burke, and Ernzerhof (PBE),[44] ensuring accurate modeling and analysis of the structural properties. The calculated bandgap is about 1.24 eV, which is close to our prior experiment results bandgap for bulk $PdBr_2$. We also present the total and partial density of states (DOS) for $PdBr_2$ in Fig. S2. Analysis of the projected DOS reveals that both the conduction and valence bands could be attributed to the contributions from both Pd and Br atoms. Scanning electron microscope image, energy dispersive spectroscopy elemental measurement results, and mapping plot are shown in Figs. 1(d) and 1(e), respectively. The Pd:Br atomic ratio as 33.46:66.54 of a typical flake sample indicates the stoichiometric ratio of 1:2. Figure 1(f) shows the non-polarized Raman spectrum of $PdBr_2$. Three phonon vibration peaks at 120 cm^{-1}–240 cm^{-1} (namely P_1, P_2, and P_3) is observed, which is in good agreement with previous investigations of Raman information on bulk $PdBr_2$ sample.[37,39]

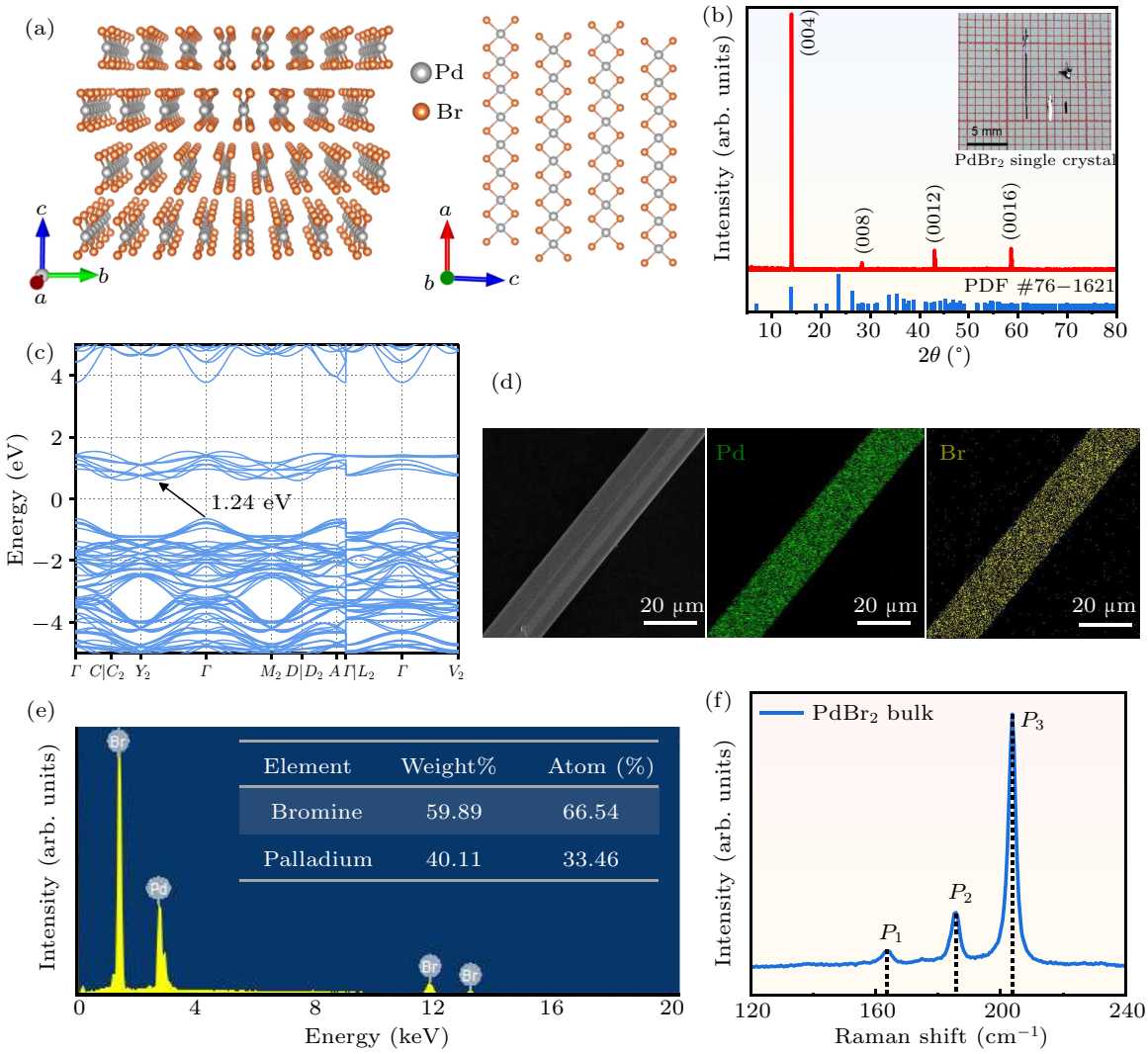


Fig. 1. (a) Atomic structure of $PdBr_2$ crystal with different views. (b) X-ray diffraction pattern of the $PdBr_2$ single crystal. The inset is optical graph of $PdBr_2$ with red lattice scale bar of 1 mm. (c) Band structure of the bulk $PdBr_2$ calculated with the PBE functional. (d) Scanning electron microscope image of a representative $PdBr_2$ flake with energy dispersive spectroscopy (EDS) mapping of the palladium and bromine elements. (e) EDS results reveal the stoichiometric ratio of $PdBr_2$. (f) Non-polarized Raman spectrum of a representative $PdBr_2$ flake.

The symmetry of chemical bond vibration and crystal orientation can be determined using ARPRS measurement.[40,41] During the measurement, the analyzer is adjusted to align parallel and perpendicular to the laser polarization direction, respectively. The incident laser (532 nm) is polarization light and fixed horizontally, with the scattered light polarization vector aligned either parallel (XX) or perpendicular (XY) to that of the incident laser using a polarization analyzer. The ARPRS experiment is performed by incrementally rotating the sample at an interval of 30°. Figures 2(a) and 2(b) give the three-dimensional (3D) contour color mapping and two-dimensional (2D) projection of polarized Raman intensity with the rotation angles ranging from 0° to 360° in XX and XY configurations, respectively. The intensity of the Raman peaks exhibits visibly discrepancy changes depending on the polarization angle θ. The bulk $PdBr_2$ crystal exhibits monoclinic symmetry with a C_{2h} point group, featuring 18 phonon modes ($3A_g + 6A_u + 3B_g + 6B_u$) at the Gamma point. Among them, six phonon modes are Raman active ($3A_g + 3B_g$). In our scheme, only A_g modes (P_1: 163 cm^{-1}, P_2: 185 cm^{-1}, P_3: 203 cm^{-1}) are observable in ARPRS due to the polarization selection rules of XX and XY configurations. The formula based on group theory and Raman tensors is utilized to fit the Raman intensity function with polarization angle[39,42]

$$I\left(A_g, \parallel\right) \propto \left[a\cos^2\theta + b\sin^2\theta + 2d\sin\theta\cos\theta\right]^2, \quad (1)$$

$$I\left(A_g, \perp\right) \propto \left[d\left(\cos^2\theta - \sin^2\theta\right) + (b-a)\cos\theta\sin\theta\right]^2. \quad (2)$$

Here, a, b, and d are the tensor constants for specific Raman mode. θ is the polarization angle. Figures 2(c)–2(e) display the polar plots for the Raman peak intensity at (c) 163 cm^{-1}, (d) 185 cm^{-1}, and (e) 203 cm^{-1} as the function of polarization angles, respectively. The fitting curves in polar coordinates using Eqs. (1) and (2) agree well with the experimental data. The phonon modes, which vary with the polarization angles, provide insights into the anisotropic structure

and enable one to determine the lattice orientation of $PdBr_2$ flake. The polar plot shows that the anisotropy variation period of the P_1 peak is 180°, while the period of P_2 and P_3 peaks is 90°. The ARPRS results reveal that the $PdBr_2$ flakes exhibit an in-plane anisotropic structure, which motivates further exploration into their in-plane anisotropic absorbance and polarization-dependent photoresponse performances.

We subsequently examine the absorption of polarized light by $PdBr_2$ when exposed to a laser beam with polarization angle ranging from 0 to 180° in an interval of 45°. The results are depicted in Fig. 3(a). The angle of polarization is determined by the disparity between the orientation of light polarization vector and the *a* axis of the $PdBr_2$ crystal, as shown in the inset of Fig. 3(a). It is found that the $PdBr_2$ flake exhibits strong polarization-angle dependence of optical absorption intensities in a broad spectral range from 200 nm to 1000 nm. Interestingly, a clear occurrence of the optical reversal phenomenon can be observed. For example, the absorption gradually increases at 755 nm and gradually decreases at 350 nm within the range of 45° to 135°. The laser power remains consistent throughout our measurement, and the observed variation in absorption intensity indicates the occurrence of the LD transition of $PdBr_2$. The LD ratio, defined as the ratio in absorption intensity parallel, and perpendicular to *a*-axis direction, is plotted in Fig. 3(b). By referring to the optical image in measurement, we choose the absorption intensities along 45° and 135° configurations, i.e., parallel and perpendicular to the *a*-axis direction, to investigate the LD of $PdBr_2$ nanoflakes. Comparisons of two kinds of dichroism ratio modes (red line, α-135°/α-45°) and (green line, α-45°/α-135°) are extracted from the absorption spectra in Fig. 3(a). The intersection occurs at a wavelength of 397 nm, referring as the reversal point. It should be noted that similar optical reversal phenomenon has also been reported in other low-dimensional materials such as $PdSe_2$,[43] SiP,[44] $Ni_2Pd_3Se_8$,[45] etc. In Fig. 3(c), the absorption intensities at different angles are compared before and after the reversal point, specifically under 350-nm and 75-nm wavelengths, which observes an approximately 90° distinct reversal. Figure 3(d) displays the polarized light absorption intensity of $PdBr_2$ crystal across a range of polarization angles from 0° to 360°. Notably, there is a clear reversal in polarized light absorption between the 350 nm and 755 nm wavelength ranges. The dichroic ratios at 350 nm and 755 nm are 1.02 and 1.78, respectively, as shown in the inset of Fig. 3(e). Above all, the $PdBr_2$ nanoflake demonstrates a significant linear dichroism effect and an intriguing optical reversal phenomenon, which could be employed for polarization-sensitive photodetection.

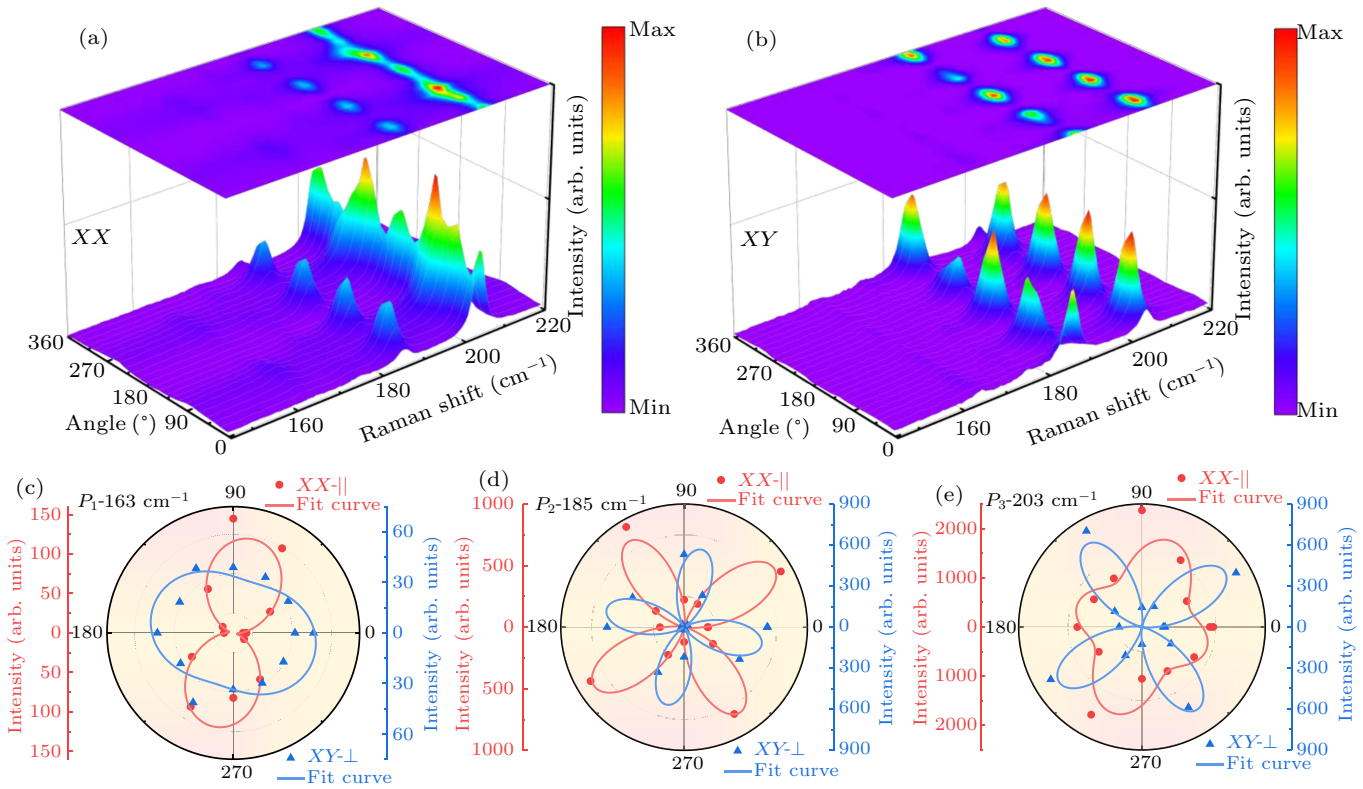


Fig. 2. Panels (a) and (b) are the 3D colormap surface plots of angle-resolved Raman spectrum with the 2D projection plot under (a) *XX* and (b) *XY* polarizations configurations, respectively. (c)–(e) Polar plots under the *XX*-parallel configuration (red dot symbolizes experiment results and red line represents fitted curve) and the *XY*-perpendicular configuration (blue triangle symbolizes experiment results and blue line represents fitted curve) with fitting to the angle-dependent Raman intensities of (c) P_1, (d) P_2, (e) P_3 modes of $PdBr_2$.

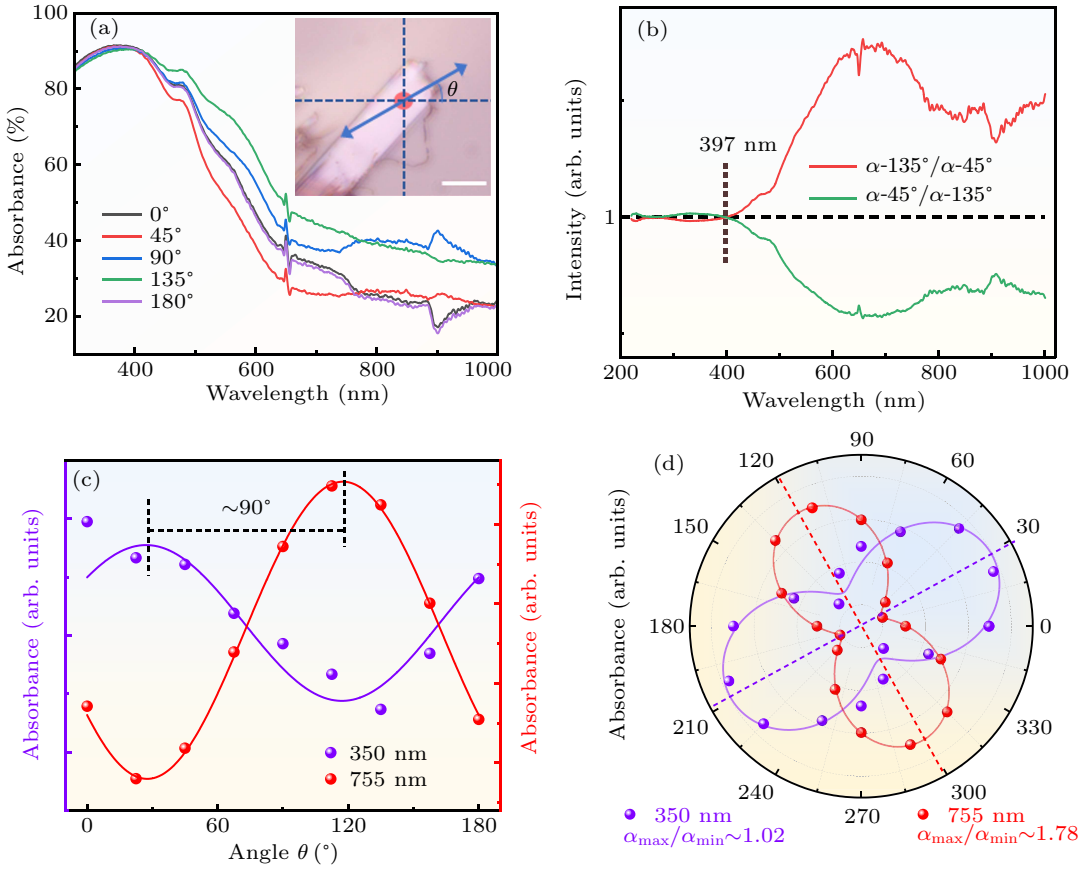


Fig. 3. (a) Polarized absorption spectra of $PdBr_2$ within the wavelength ranges of 200 nm–1000 nm collected under polarization angles from 0° to 180°. (b) The linear dichroic ratios extracted from panel (a). (c) The variation of absorption intensity with angle at two different wavelengths (350 nm and 755 nm), exhibiting perpendicular optical reversal. (d) Evolution of absorbances with angle in the polar coordinate at 350 nm and 755 nm, respectively. The corresponding absorption ratio is labeled in the bottom corner.

In order to explore the optoelectronic characteristics of $PdBr_2$ nanowire, we build a two-terminal device using an individual $PdBr_2$ nanowire on an SiO_2/Si substrate (300 nm in depth). The scheme is illustrated in Fig. 4(a). Figure 4(b) shows the dark field optical microscopy (OM) image of the $PdBr_2$ nanowire device. And the inset of Fig. 4(b) is the bright OM image of the same device. According to previous report,[39] similar device exhibits prominent photoresponse under 405-nm light irradiation. Thus, we primarily study the optoelectrical performances of the photodetector under 405-nm light irradiation. As shown in Fig. 4(c), there is a small Schottky barrier between the electrode and $PdBr_2$ channel material. We also present the I_{ds}–V_{ds} responses using linear coordinates in Fig. S3. The observed asymmetry in the I_{ds}–V_{ds} curves can be attributed to barriers or inherent asymmetries in charge transport. And the photoresponse of $PdBr_2$ nanowire device increases with the increase of V_{ds} under the illumination of different power density. The photocurrent ($I_{ph} = I_{light} - I_{dark}$) increases gradually with increasing of the illuminated power density. The low power density of 0.002 mW·mm^{-2} produces a photocurrent of 1.1 nA at a bias voltage of 3 V, which is about an order of magnitude larger than that under dark condition. Figure 4(d) plots the relationship of I_{ph} with the illuminated power densities (P) at the bias voltage of 3 V. A sublinear photoresponse is observed, and it can be fitted using the power law relation $I_{ph} \propto P^{\alpha}$. Generally, the power exponent α is close to 1, demonstrating the photoconduction mechanism of the photodetector. The presence of a value smaller than 1 may be attributed to the intricate dynamics of carrier generation, trapping, and recombination processes. In the present case, the small value of $\alpha = 0.14$ suggests that the dominant factor influencing the photocurrent generation in $PdBr_2$ nanowire photodetector is the photogating effect.

We proceed to calculate the responsivity (R) and detectivity (D^*) of the device at 405-nm wavelength using the equations

$$R = I_{ph}/(PA), \tag{3}$$

$$D^* = RA^{1/2}/(2eI_{dark})^{1/2}, \tag{4}$$

where I_{ph}, P, A, e, and I_{dark} are the photocurrent, power density, effective area of the device ($\sim 0.73\ \mu m^2$), electron charge, and the device current under dark, respectively. The calculated R and D^* as the functions of power density are presented in Fig. 4(e). It is found that the responsivity R and detectivity D^* can reach 747 A·W^{-1} and 5.8×10^{12} Jones at $V_{ds} = 3$ V

and $P = 0.002$ mW·mm^{-2}, respectively. Figure 4(f) shows the photoresponse speed of the photodetector, where the rise time (τ_{rise}) and decay time (τ_{decay}) are defined as the duration time for the photocurrent to increase from 10% to 90% and decrease from 90% to 10%, respectively. The time-resolved photoresponses with 10 cycles observed under periodic illumination at 405-nm wavelength are displayed in Fig. S4. The obtained τ_{rise} and τ_{decay} are 0.13 s and 5.19 s, respectively. The longer decay time comparing to the rise time is attributed to the existence of electron–hole trapping states, which prevent the recombination of charge carriers. The presence of trapping states within the material could enhance the photoconductivity of the device. This behavior also confirms that the optoelectronic mechanism in the $PdBr_2$ photodetector device is the photogating effect. We present the wavelength-dependent responsivity of a $PdBr_2$ photodetector covering a range of wavelengths from 405 nm to 940 nm in Fig. S5. It can be found that the responsivity at 405 nm wavelength is remarkably larger than that in other wavelengths, which is attributed to the bandgap and absorption characteristics of $PdBr_2$.

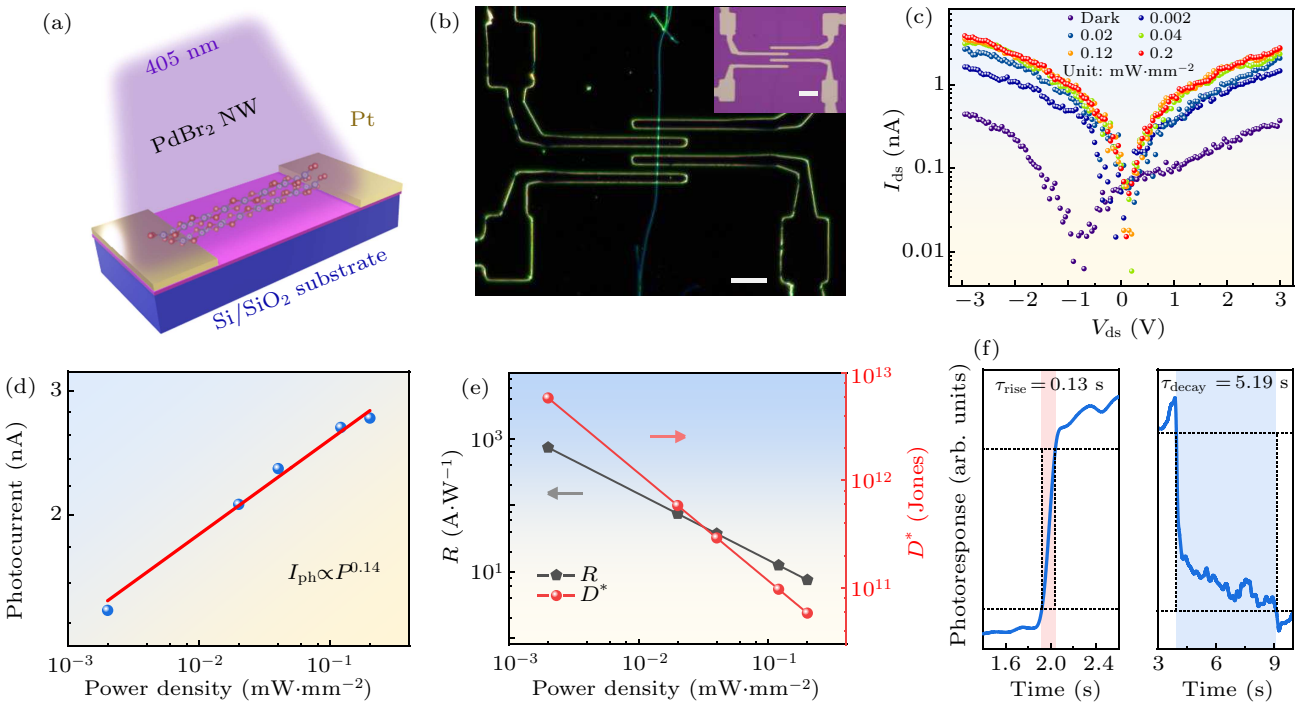


Fig. 4. (a) Scheme illustration of the $PdBr_2$ nanowire photodetector. (b) Dark field optical microscopy (OM) image of a $PdBr_2$ nanowire device. The inset is the corresponding bright-field OM image. The scalebar is 10 μm. (c) I_{ds}–V_{ds} responses of the photodetector under dark and 405-nm laser illumination at different power densities. (d) The correlation between the power density and the resulting photocurrent responses, which are extracted under a bias voltage of 3 V from panel (c). (e) Responsivity (R) and specific detectivity (D^*) of the $PdBr_2$ photodetector at different power densities. (f) Typical temporal photoresponses of the $PdBr_2$ nanowire photodetector under 0.2-mW·mm^{-2} illumination.

In view of the intrinsic structural anisotropy of $PdBr_2$, we conduct the study on the anisotropic photoresponses of $PdBr_2$ nanowire photodetector by measuring the polarization-dependent photodetection. Figure 5(a) shows the scheme of the polarized photodetection, where a Glan–Taylor prism and a half-wave plate are utilized to generate linearly polarized light. By switching the on and off state of the laser (405 nm) and synchronously adjusting the polarization angle (θ) of the polarized light from 0° to 360° at a step of 20°, the dynamic photoresponses of the $PdBr_2$ nanowire device are continuously monitored. The photodetector exhibits a periodic photoresponse with a period of 180°. The lowest and highest photocurrents are observed when the light is aligned to be parallel and perpendicular to the a-axis direction of $PdBr_2$ nanowire, respectively. The function $I_{ph} = I_{pha}\cos^2(\theta) + I_{phb}\sin^2(\theta)$ provides a good fit for the photocurrent values with respect to polarization angle θ. A high photocurrent anisotropy ratio (I_{ph-max}/I_{ph-min}) of 1.56 has been achieved. The polar diagram in Fig. 5(c) displays the normalized photocurrent distribution. The results indicate a high polarization sensitive photodetector based on $PdBr_2$ nanowire. Figure 5(d) summarizes the wavelength range and the anisotropic ratio of previously reported polarization sensitive photodetectors built of various nanowire and nanobelt materials.[45–56] It is found that the $PdBr_2$ nanowire photodetector exhibits the optimal anisotropic optoelectronic performance at the near-ultraviolet (405 nm) region. The remarkable polarization-sensitive performance of the $PdBr_2$ nanowire photodetector holds great promise for designing multifunctional optoelectronic devices and facilitating their integration and miniaturization.

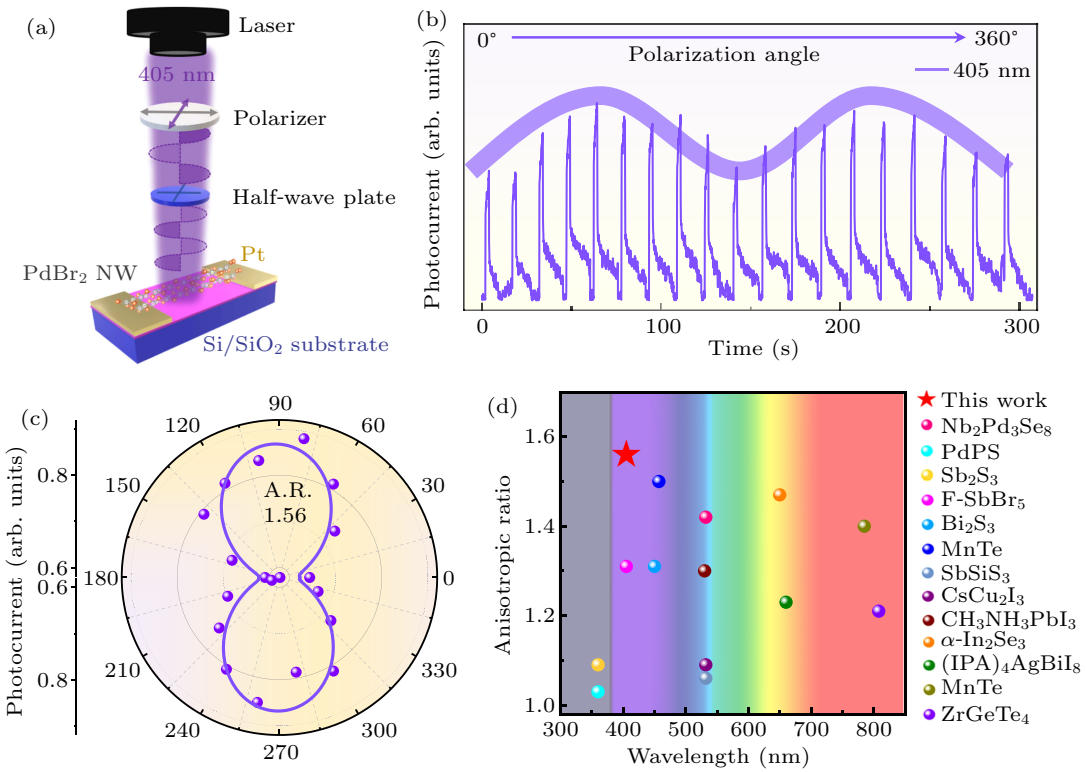


Fig. 5. (a) Schematic diagram of $PdBr_2$ nanowire polarization photodetector. (b) The photoresponses of the photodetector device under on and off switching. The polarization angle is rotated from 0° to 360° at a step of 20°. (c) Polar diagram illustrating the photocurrent response at different angles when exposed under a 405-nm light. (d) Comparisons of the photocurrent anisotropic ratio and photoresponse range with other typical 2D and 1D materials.

4. Conclusion

In conclusion, optical reversal of linear dichroism has been established in $PdBr_2$, a quasi-one-dimensional material with in-plane anisotropic structure. The $PdBr_2$ nanowire photodetector exhibits high performance with a responsivity of 746 $A{\cdot}W^{-1}$ and a detectivity of 5.8×10^{12} Jones, respectively. Moreover, the photodetector demonstrates polarization sensitivity with large photocurrent anisotropy ratio of 1.56. This work demonstrates that $PdBr_2$ can be applied to realize high-performance polarized photodetectors, broadening the application in high sensitivity and polarization-resolved photodetection and imaging applications.

Acknowledgements

Project supported by the National Key Research and Development Program of China (Grant Nos. 2022YFA1403203 and 2021YFA1600201), the National Natural Science Foundation of China (Grant No. 12274414), and the Basic Research Program of the Chinese Academy of Sciences Based on Major Scientific Infrastructures (Contract No. JZHKYPT-2021-08).

References

[1] Wang G, Wang R, Kong W and Zhang J 2018 *Cogn. Neurodynamics* **12** 615
[2] Bass M, DeCusatis C, Enoch J, Lakshminarayanan V, Li G, MacDonald C, Mahaja V and Van Stryland E 2009 *Handbook of Optics, 3rd IV: Optical Properties of Materials, Nonlinear Optics* (McGraw-Hill)
[3] McCormick G C and Hendry A 1975 *Radio Sci.* **10** 421
[4] Xin W, Zhong W, Shi Y, Shi Y, Jing J, Xu T, Guo J, Liu W, Li Y, Liang Z, Xin X, Cheng J, Hu W, Xu H and Liu Y 2024 *Adv. Mater.* **36** 2306772
[5] Wang X, Zhong F, Kang J, Liu C, Lei M, Pan L, Wang H, Wang F, Zhou Z, Cui Y, Liu K, Wang J, Shen G, Shan C, Li J, Hu W and Wei Z 2021 *Sci. China Mater.* **64** 1230
[6] Wolff L B 1997 *Image and Vision Computing* **15** 81
[7] Sakamoto M, Ono Y, Noda K, Sasaki T, Kawatsuki N, Tanaka M and Ono H 2024 *Opt. Commun.* **552** 130118
[8] Huang X, Wu C, Xu X, Wang B, Zhang S, Shen C, Yu C, Wang J, Chi N, Yu S and Chang-Hasnain C J 2023 *Nat. Commun.* **14** 6855
[9] Wang B, Tang Z, Zheng H, Wang L, Wang Y, Wang R, Qiu Z and Zhu H 2023 *Chin. Phys. B* **32** 098508
[10] Ran W, Ren Z, Wang P, Yan Y, Zhao K, Li L, Li Z, Wang L, Yang J, Wei Z, Lou Z and Shen G 2021 *Nat. Commun.* **12** 6476
[11] Wu S, Chen Y, Wang X, Jiao H, Zhao Q, Huang X, Tai X, Zhou Y, Chen H, Wang X, Huang S, Yan H, Lin T, Shen H, Hu W, Meng X, Chu J and Wang J 2022 *Nat. Commun.* **13** 3198
[12] Wan P, Jiang M, Su L, Xia S, Wei Y, Xu T, Liu Y, Shi D, Fang X and Kan C 2022 *Adv. Funct. Mater.* **32** 2207688
[13] Wang F, Hu F, Dai M, Zhu S, Sun F, Duan R, Wang C, Han J, Deng W, Chen W, Ye M, Han S, Qiang B, Jin Y, Chua Y, Chi N, Yu S, Nam D, Chae S H, Liu Z and Wang Q J 2023 *Nat. Commun.* **14** 1938
[14] Zhou Z, Cui Y, Tan P, Liu X and Wei Z 2019 *J. Semicond.* **40** 061001
[15] Yu Y F, Zhang Y, Zhong F, Bai L, Liu H, Lu J P and Ni Z H 2022 *Chin. Phys. Lett.* **39** 058501
[16] Han J, Wang F, Zhang Y, Deng W, Dai M, Hu F, Chen W, Cui J, Zhang C, Zhu S, Wang C, Ye M, Han S, Luo Y, Zhai T, Wang J and Wang Q J 2023 *Adv. Mater.* **35** 2305594
[17] Li C, Wu Z, Zhang C, Peng S, Han J, He M, Dong X, Gou J, Wang J and Jiang Y 2023 *Adv. Opt. Mater.* **11** 2300905
[18] Pi L, Wang P, Liang S J, Luo P, Wang H, Li D, Li Z, Chen P, Zhou X, Miao F and Zhai T 2022 *Nat. Electron.* **5** 248
[19] Wang H, Li Y, Gao P, Wang J, Meng X, Hu Y, Yang J, Huang Z, Gao W, Zheng Z, Wei Z, Li J and Huo N 2024 *Adv. Mater.* **36** 2309371

[20] Wang W, Sun Y, Dai P, Gao H, Du C and Li K 2023 *Appl. Phys. Lett.* **122** 233101
[21] Chen Y, Su L, Jiang M and Fang X 2022 *J. Mater. Sci. Technol.* **105** 259
[22] Yao H, Guo X, Bao A, Mao H, Ma Y and Li X 2022 *Chin. Phys. B* **31** 038501
[23] Jiang J, Xu T, Lu J, Sun L and Ni Z 2019 *Research* **2019** 4641739
[24] Lian W, Jiang C, Yin Y, Tang R, Li G, Zhang L, Che B and Chen T 2021 *Nat. Commun.* **12** 3260
[25] Wang J, Fang H, Wang X, Chen X, Lu W and Hu W 2017 *Small* **13** 1700894
[26] Chen X, Chen B, Jiang B, Gao T, Shang G, Han S T, Kuo C C, Roy V A L and Zhou Y 2023 *Adv. Funct. Mater.* **33** 2208807
[27] Jia C, Lin Z, Huang Y and Duan X 2019 *Chem. Rev.* **119** 9074
[28] Anttu N, Abrand A, Asoli D, Heurlin M, Åberg I, Samuelson L and Borgström M 2014 *Nano Res.* **7** 816
[29] Otnes G and Borgström M T 2017 *Nano Today* **12** 31
[30] Nehra M, Dilbaghi N, Marrazza G, Kaushik A, Abolhassani R, Mishra Y K, Kim K H and Kumar S 2020 *Nano Energy* **76** 104991
[31] Yu Y, Hu Y, Yang J and Wei Z 2022 *Mater. Today Electron.* **2** 100013
[32] Tien L C, Shih Y C, Chen C Y, Huang Y T and Chen R S 2021 *J. Alloys Compd.* **876** 160195
[33] Yan X, Zhen W L, Hu H J, Pi L, Zhang C J and Zhu W K 2021 *Chin. Phys. Lett.* **38** 068103
[34] Ding H, Liu W, Zheng Y, Li C, Jiang H and Wang X 2019 *J. Mater. Chem. C* **7** 1690
[35] Manser J S, Christians J A and Kamat P V 2016 *Chem. Rev.* **116** 12956
[36] Jiang S, Li L, Wang Z, Mak K F and Shan J 2018 *Nat. Nanotechnol.* **13** 549
[37] Liu H, Wang X, Wu J, Chen Y, Wan J, Wen R, Yang J, Liu Y, Song Z and Xie L 2020 *ACS Nano* **14** 10544
[38] Cui Q, Liang J, Yang B, Wang Z, Li P, Cui P and Yang H 2020 *Phys. Rev. B* **101** 214439
[39] Fu L, Shang C, Zhou S, Guo Y and Zhao J 2022 *Appl. Phys. Lett.* **120** 023103
[40] Mak K F, Shan J and Ralph D C 2019 *Nat. Rev. Phys.* **1** 646
[41] Das B, Dolui K, Paramanik R, Kundu T, Maity S, Ghosh A, Palit M and Datta S 2023 *Appl. Phys. Lett.* **122** 263504
[42] Chen M M, Li S S, Ji W X and Zhang C W 2023 *Chin. Phys. B* **32** 127103
[43] Zhu W, Zhen W, Niu R, Jiao K, Zhang R, Zhang L, Xue F and Zhang C 2023 *ACS Photon.* **10** 4465
[44] Perdew J, Burke K and Ernzerhof M 1996 *Phys. Rev. Lett.* **77** 3865
[45] Lei Z, Zhang X, Zhao Y, Wei A, Tao L, Yang Y, Zheng Z, Tao L, Yu P and Li J 2022 *Nanoscale* **14** 4181
[46] Taghizadeh A, Leffers U, Pedersen T G and Thygesen K S 2020 *Nat. Commun.* **11** 3011
[47] Li L, Gong P, Sheng D, Wang S, Wang W, Zhu X, Shi X, Wang F, Han W, Yang S, Liu K, Li H and Zhai T 2018 *Adv. Mater.* **30** 1804541
[48] Yu J, Kuang X, Gao Y, Wang Y, Chen K, Ding Z, Liu J, Cong C, He J, Liu Z and Liu Y 2020 *Nano Lett.* **20** 1172
[49] Xie X, Ding J, Wu B, Zheng H, Li S, Wang C T, He J, Liu Z, Wang J T, Duan J A and Liu Y 2023 *Nanoscale* **15** 12388
[50] Qin Q, Gao W, Zhang H, Chen J, Yan Y, Zhu K, Long M, Li G, Yin S, Du Y, Zhang H, Wang Q, Wang Z, Li Y, Wang S and Li L 2023 *J. Mater. Chem. A* **11** 11517
[51] Li G, Chen Z, Zhang H, Yu M, Zhang H, Chen J, Wang Z, Yin S, Lin W, Gong P, Zeng L, Zhu X, Wei W, Tian M and Li L 2022 *Nanoscale* **14** 14129
[52] Zhang S, Wang H, Kirchner M M, Liu J, Luo H, Ren Y, Yuan C, Hattori H T, Miroshnichenko A E and Lei W 2022 *Adv. Mater. Interfaces* **9** 2200448
[53] Zhang W, Hong M and Luo J 2021 *J. Am. Chem. Soc.* **143** 16758
[54] Yi H, Ma C, Wang W, Liang H, Cui R, Cao W, Yang H, Ma Y, Huang W, Zheng Z, Zou Y, Deng Z, Yao J and Yang G 2023 *Mater. Horiz.* **10** 3369
[55] Ye K, Yan J, Liu L, Li P, Yu Z, Gao Y, Yang M, Huang H, Nie A, Shu Y, Xiang J, Wang S and Liu Z 2023 *Small* **19** 2300246
[56] Yang W, Xiong T, Liu Y Y, Yang J, Xu Q and Wei Z 2022 *Small Structures* **3** 2200061
[57] Li Y, Ma J, Liang W, Tian Y, Li X, Wu D, Shi Z and Fang X 2023 *Chem. Eng. J.* **451** 138531
[58] Gou R, Shi C, Zhou S, Huang Z, Ouyang Z, He S, Zhao J, Xiao Y, Lei S and Cheng B 2023 *ACS Appl. Mater. Interfaces* **15** 54863
[59] Wang S, Yang Z, Wang D, Tan C, Yang L and Wang Z 2023 *ACS Appl. Mater. Interfaces* **15** 3357
[60] Li Z, Chen Q, Wang Z, Fan Y, Zhu T, Ji C, Kuang X and Luo J 2022 *J. Mater. Chem. C* **10** 18063
[61] Bai R, Xiong T, Zhou J, Liu Y Y, Shen W, Hu C, Yan F, Wang K, Wei D, Li J, Yang J and Wei Z 2022 *InfoMat* **4** e12258